Schweizerischer Erdbebendienst
Service Sismologique Suisse
Servizio Sismico Svizzero
Servizi da Terratrembels Svizzer

ETH
Eidgenössische Technische Hochschule Zürich
Swiss Federal Institute of Technology Zurich

Buchs - Altendorf (SBUA2)

SITE CHARACTERIZATION REPORT

Clotaire MICHEL, Carlo CAUZZI, Valerio POGGI

Daniel ROTEN, Jan BURJANEK, Donat FÄH

Sonneggstrasse 5 CH-8092 Zürich Switzerland; E-mail: clotaire.michel@sed.ethz.ch

Last modified : November 5, 2013

Abstract

Site characterization using ambient vibration single station and array measurements was performed on the alluvial fan of Buchs Altendorf. The site is hosting the station SBUA2 of the Swiss Strong Motion Network, which replaces the station SBUA from the old network. In order to map the bedrock depth in the area, a single station survey with H/V analysis was performed. In order to characterize the velocity profile under the station, two array configurations were used, including a large array of $200\,\mathrm{m}$ aperture recording overnight. The measurements were useful to derive a velocity model for this alluvial fan and a comparison with borehole data could be done. At the central point of the array, we found a gradually increasing velocity with depth down to $50\,\mathrm{m}$ from 150 to $1300\,\mathrm{m/s}$ without clear layering corresponding to more and more consolidated gravels. At this depth, a layer with constant velocity (around $1300\,\mathrm{m/s}$) is found down to the bedrock at $90\,\mathrm{m}$. The derived layers down to $90\,\mathrm{m}$ depth are very stiff and explain the H/V peak around $4\,\mathrm{Hz}$ that corresponds to the fundamental SH resonance frequency, but not the ellipticity. $V_{s,30}$ is found to be close to $620\,\mathrm{m/s}$. A site to reference analysis from the array data shows 3 amplification peaks between 4 and $8\,\mathrm{Hz}$. The first is related to the interface with the bedrock. The second and eventually the third are producing the largest amplifications up to 7 under ambient vibrations in the Fourier domain (5 close to SBUA2) and are related to shallower layers. Comparing with the SH transfer function and using polarization analysis, it is shown that part of the recorded motion is due to a local 2D resonance.

Contents

1 Introduction

The station SBUA2 (Buchs Altendorf) is part of the Swiss Strong Motion Network (SSMNet) in the Rhine valley. The local network comprises a rock site (station SBUB) and two sedimentary sites (SBUA2 and SBUH). Former station SBUA was renewed in the framework of the SSMNet Renewal project as SBUA2 station in June 2011. The former SBUA station was located at a basin edge, close to the outcropping bedrock. The new station SBUA2 was shifted to the centre of the alluvial fan in order to avoid recordings of complex wave reflections on the basin edge. The project includes also the site characterization. The passive array measurement has been selected as a standard tool to investigate these sites. The measurement campaign was done on 20st July 2010 in Buchs Altendorf (Fig. 1), with a centre close to station SBUA2, in order to characterize the alluvial fan under this station. In addition to these passive array measurements, a single station measurement campaign had to be performed in order to better understand the spatial distribution of the bedrock depth. Moreover, 2 profiles across the valley were done in order to understand the shape of the valley and better select a site for the replacement of station SBUG. This second measurement campaign was performed between August 23rd and 26th 2010 by M. Terzic (Fig. 1). This report presents the measurement setups, the results of the H/V analysis, including the fundamental frequencies and of the array processing of the surface waves (dispersion curves). Then, an inversion of these results for a velocity profile is performed. It also gives the results of site to reference spectral ratios that could be performed using the array data. Boreholes are also presented and all these data are interpreted to fully characterize the site.

Canton	City	Location	Station code	Site type	Slope
St Gallen	Buchs	Altendorf	SBUA2	Alluvial fan	Flat

Table 1: Main characteristics of the study-site.

Figure 1: Picture of the site for the first and second measurement campaign.

2 Experiment description

2.1 Ambient Vibrations

The ground surface is permanently subjected to ambient vibrations due to:

- natural sources (ocean and large-scale atmospheric phenomena) below $1\,\mathrm{Hz}$,
- local meteorological conditions (wind and rain) at frequencies around $1\,\mathrm{Hz}$,
- human activities (industrial machines, traffic…) at frequencies above $1\,\mathrm{Hz}$ [Bonnefoy-Claudet et al., 2006].

The objective of the measurements is to record these ambient vibrations and to use their propagation properties to infer the underground structure. First, the polarization of the recorded waves (H/V ratio) are used to derive the resonance frequencies of the ground layers for single stations. Second, the arrival time delays between stations is used to derive the velocity of surface waves at different frequencies (dispersion) for array recordings. The information (H/V, dispersion curves) is then used to derive the properties of the soil layers using an inversion process.

2.2 Equipment

For the first measurement 12 Quanterra Q330 dataloggers named NR01 to NR12 and 14 Lennartz 3C 5 s seismometers were available (see Tab. 2). Each datalogger can record on 2 ports A (channels EH1, EH2, EH3 for Z, N, E directions) and B (channels EH4, EH5, EH6 for Z, N, E directions). The time synchronization was ensured by GPS. The sensor are placed on a metal tripod in a $20\,\mathrm{cm}$ hole, when possible, for a better coupling with the ground.
For the second experiment, 1 Nanometrics Taurus datalogger and 1 Lennartz 3C 5 s seismometer were used (see Tab. 2). The time was not synchronized on GPS and may suffer from a shift of several tenths of seconds. The sensor are placed directly on the ground (generally road) and leveled using the screws. A laptop with a seedlink server could be linked to the datalogger and stream the data. They could therefore be read by the Geopsy software `http://www.geopsy.org` and the processing made near real-time. It allowed therefore to have an idea of the results directly on the field, refine the measurement grid where it was necessary, record more time if necessary etc.

Digitizer	**Model**	**Number**	**Resolution**
	Quanterra Q330	12	$24\,\mathrm{bits}$
	Nanometrics Taurus	1	$24\,\mathrm{bits}$
Sensor type	**Model**	**Number**	**Cut-off frequency**
Velocimeter	Lennartz 3C	14	$0.2\,\mathrm{Hz}$
Velocimeter	Lennartz 3C	1	$0.2\,\mathrm{Hz}$

Table 2: Equipment used.

2.3 Geometry of the experiments

For the first measurement, two array configurations of simultaneous recordings were used, for a total of 4 rings of 10, 25, 50 and 100 m radius around a central station. The first configuration includes the 3 inner rings with 14 sensors; the second configuration includes the 2 outer rings with 11 sensors and was performed during the night. The minimum inter-station distance and the aperture are therefore 10 and 100 m and 50 and 200 m, respectively.

For the second campaign, a grid of 12 points around the station SBUA2, completing the 20 points of the array already done were recorded (Fig. 3). Moreover, two cross-sections of the valley of 8 and 10 points, respectively, were performed.

The experimental setups are displayed in Fig. 2. The final usable datasets are detailed in section 3.2.

Figure 2: Geometry of the arrays of the first campaign (left) and single points recorded during the second campaign (right).

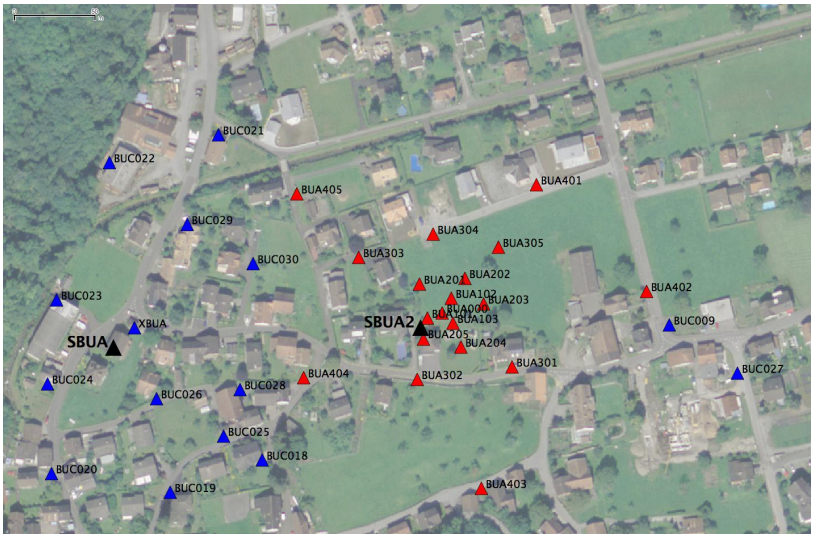

Figure 3: All available points for single station measurement around station SBUA2 including the first (red) the second (blue) campaign.

2.4 Positioning of the stations

For the first campaign, The sensor coordinates were measured using a differential GPS device, including a base station and a rover. It allows a relative positioning with an accuracy of about $10\,\mathrm{cm}$ and an absolute positioning of 1 to $5\,\mathrm{m}$. The exported positions in the WGS84 system were converted to CH1903 using the REFRAME online service of Swisstopo.

The GPS coverage was very bad. The differential GPS measurement was performed for the 1st experiment but point BUA205 had a too poor accuracy and was redone during the second experiment. The 2nd measurement of the positions was done the following morning together with point BUA205. For this point, the measurement was taken $3\,\mathrm{m}$ to the W because there were too many trees. Since the 2nd measurement was more accurate, it was taken as a reference. The common points with the 1st measurement (ring 3 and central station) were used to adjust the first measurement.

For the second campaign, the positioning of the stations was done by picking points on the Swissimage of Swisstopo. It allows a positioning with an accuracy of about $2\,\mathrm{m}$.

3 Data quality

3.1 Usable data

For the first campaign, the largest time windows were extracted, for which all the sensors of the array were in position and the GPS synchronization was ensured. Station NR02 (point BUA303) did not synchronize during the 2 experiments (only 5 min of synchronization) probably due to the GPS antenna and its internal battery (station is no more able to store time). It is processed only for the H/V and not for the array. Moreover, there is a problem in the Miniseed file for station NR07 channel EH1 during the night (00:18) so that this experiment is split in 2 chunks of approximately 3 hours.

For the second campaign, the largest time windows were extracted, for which the sensor was in place. The noise level is large on average since the site is located in a city.

The characteristics of the datasets are detailed in Tab. 3.

3.2 Data processing

The data were first converted to SAC format including in the header the coordinates of the point (CH1903 system), the recording component and a name related to the position. The name is made of 3 letters characterizing the location (BUA for the first and BUC for the second campaign) and 3 digits. For the first measurement, 1 digit for the circle and 2 more digits for the number in the circle are used. The response of the sensor was not corrected and the values (in counts) were not converted to $\mathrm{m/s}$.

Dataset	Starting Date	Time	Length	F_s	Min. inter-distance	Aperture	# of points
bua1	2010/07/20	16:03	88 min	200 Hz	10 m	100 m	13
bua2	2010/07/20	21:13	184 min	200 Hz	50 m	200 m	10
bua3	2010/07/21	00:20	155 min	200 Hz	50 m	200 m	10
buc1	2010/08/23	07:45	38 min	200 Hz			1
buc2	2010/08/23	08:47	41 min	200 Hz			1
buc3	2010/08/23	10:37	40 min	200 Hz			1
buc4	2010/08/23	11:34	39 min	200 Hz			1
buc5	2010/08/23	12:27	35 min	200 Hz			1
buc6	2010/08/23	13:25	38 min	200 Hz			1
buc7	2010/08/23	14:26	38 min	200 Hz			1
buc8	2010/08/23	15:17	33 min	200 Hz			1
buc9	2010/08/24	08:27	16 min	200 Hz			1
buc10	2010/08/24	09:29	31 min	200 Hz			1
buc11	2010/08/24	10:22	27 min	200 Hz			1
buc12	2010/08/24	11:08	42 min	200 Hz			1
buc13	2010/08/24	12:23	35 min	200 Hz			1
buc14	2010/08/24	13:17	29 min	200 Hz			1
buc15	2010/08/24	14:07	25 min	200 Hz			1
buc16	2010/08/24	14:46	20 min	200 Hz			1
buc17	2010/08/25	07:01	34 min	200 Hz			1
buc18	2010/08/25	07:51	33 min	200 Hz			1
buc19	2010/08/25	08:40	26 min	200 Hz			1
buc20	2010/08/25	09:21	35 min	200 Hz			1
buc21	2010/08/25	11:44	33 min	200 Hz			1
buc22	2010/08/25	12:36	31 min	200 Hz			1
buc23	2010/08/25	13:29	29 min	200 Hz			1
buc24	2010/08/25	14:17	33 min	200 Hz			1
buc25	2010/08/25	15:13	32 min	200 Hz			1
buc26	2010/08/25	17:25	23 min	200 Hz			1
buc27	2010/08/26	07:00	32 min	200 Hz			1
buc28	2010/08/26	07:49	34 min	200 Hz			1
buc29	2010/08/26	08:40	34 min	200 Hz			1
buc30	2010/08/26	09:29	29 min	200 Hz			1

Table 3: Usable datasets.

4 H/V processing

4.1 Processing method and parameters

In order to process the H/V spectral ratios, several codes and methods were used. The classical H/V method was computed using the Geopsy `http://www.geopsy.org` software. It averages the ratio of the smoothed Fourier Transform of selected time windows. Tukey windows (cosine taper of 5% width) of $50\,\mathrm{s}$ long overlapping by 50% were selected. The smoothing was done using the Konno and Ohmachi [1998] procedure with a b value of 80. The classical method computed using the method of Fäh et al. [2001] was also performed

Moreover, the time-frequency analysis method [Fäh et al., 2009] was used to estimate the ellipticity function more accurately using the Matlab code of V. Poggi. In this method, the time-frequency analysis using the Wavelet transform is computed for each component. For each frequency, the maxima in time (10 per minute with at least $0.1\,\mathrm{s}$ between each) in the TFA are determined. The Horizontal to Vertical ratio of amplitudes for each maxima is then computed and statistical properties for each frequency are derived. The used wavelet is a Cosine wavelet with parameter 9. The mean of the distribution for each frequency is kept. For comparison purposes, the time-frequency analysis by Fäh et al. [2001], based on the spectrogram, was also used, as well as the wavelet-based TFA coded in Geopsy.

The ellipticity extraction using the Capon analysis [Poggi and Fäh, 2010] was also performed.

Method	Freq. band	Win. length	Anti-trig.	Overlap	Smoothing
Standard H/V Geopsy	$1-20\,\mathrm{Hz}$	$50\,\mathrm{s}$	No	50%	K&O 80
Standard H/V D: Fäh	$1-20\,\mathrm{Hz}$	$30\,\mathrm{s}$	No	75%	?
H/V TFA Geopsy	$1-20\,\mathrm{Hz}$	Morlet m=8 fi=1	No	-	?
H/V TFA D. Fäh	$1-20\,\mathrm{Hz}$	Specgram	No	-	?
H/V TFA V. Poggi	$1-20\,\mathrm{Hz}$	Cosine wpar=9	No	-	No

Table 4: Methods and parameters used for the H/V processing.

4.2 Results

Stability in the array

According to the standard H/V method (Fig. 4), close to the central station, the H/V peaks are very clear and consistent at frequency of $3.6-4\,\mathrm{Hz}$ with amplitudes of 3 to 5. The frequency decreases to the Northwest down to $3.2\,\mathrm{Hz}$ at the extreme point of the array in that direction (Fig. 5). To the Southeast, the frequencies are increasing slightly up to $4.7\,\mathrm{Hz}$ (point BUA404). The situation is similar when going to the East (point 405), up to $6.3\,\mathrm{Hz}$ at the former strong motion station. In the South, point BUA403 shows only a H/V peak at high frequency $18\,\mathrm{Hz}$ indicating that it is already on rock. The H/V curve of points BUA301, BUA302, BUA402, dashed in Fig. 4, are more flat and the peaks are not clear, providing large differences depending on the analysis code. The quality of H/V point BUA204 is bad.

According to the H/V time-frequency analysis, the distribution of the points is similar with generally lower frequency values in frequency and amplitude for the peaks. Points 103, 202 and 204 were removed from the analysis because of a low-frequency noise source, probably due to bad coupling, that hides the right peaks. The comparison between the two methods is confirming these statements (Fig. 6). Moreover, all the methods to compute H/V ratios are compared on Fig. 7, in which the classical methods were arbitrary divided by $\sqrt{2}$. The matching above the resonance frequency is almost perfect except smoothing issues.

Distribution of H/V peak in the area

Fig. 8 and Fig. 9 show the maps of the fundamental frequencies derived from the ellipticity of the recordings. On the alluvial fan, the situation is complex and needs more data to be interpreted (see section 4.4). In the valley, the structures are following the valley with resonance frequencies from 2 to $0.5\,\mathrm{Hz}$. An array should be performed in this part when the site for the replacement of station SBUG will be found. This study shows however that the location of SBUG can be changed without large differences in the soil response.

These frequency peaks were interpolated on QGIS using the Inverse Distance Weighting (IDW) and the linear Triangular Interpolation (TIN) algorithms. A E-W cross-section (IDW algorithm) in the South of the studied zone and a SW-NE cross-section (TIN algorithm) are presented on Fig. 10. It shows the continuous decrease of the resonance frequencies. In the cross-section, it is disturbed by the outcropping rock. The resonance frequencies go from 12 in the edges down to $0.5\,\mathrm{Hz}$ in the central part. These very low values are comparable to those found downstream in other tests. The cross-sections of the valley show iso-frequence parallel to the valley, only disturbed by the outcropping bedrock in the basin edges.

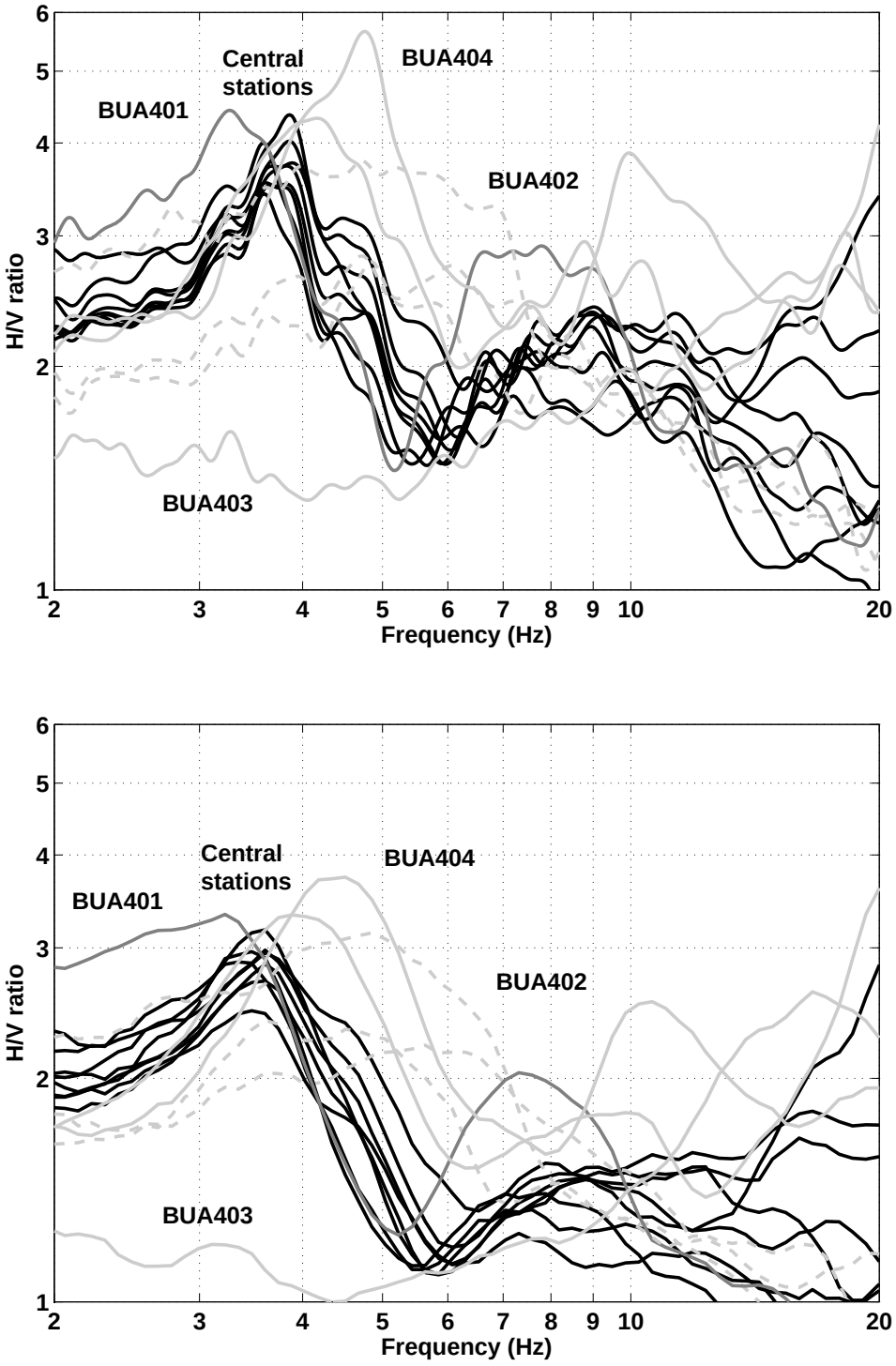

Figure 4: H/V spectral ratios (standard method using Geopsy (top) and time-frequency analysis code V. Poggi (bottom). Black: curves similar to the central station, light gray: upper frequency peaks, dark gray: lower frequency peak.

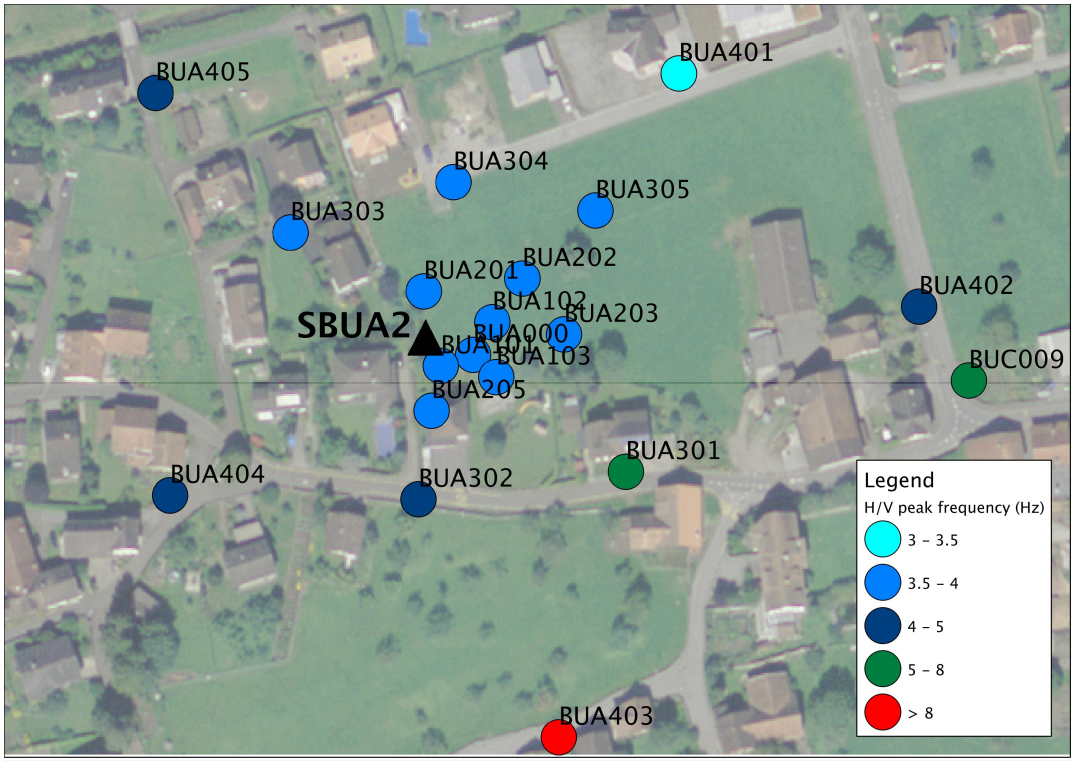

Figure 5: Map of the resonance frequencies in the array

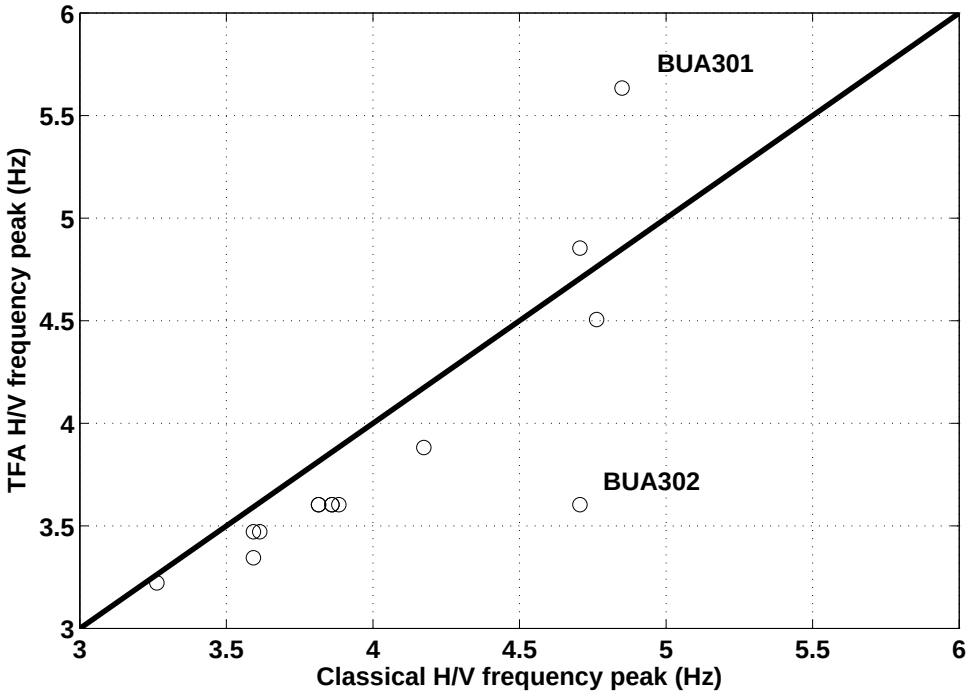

Figure 6: Comparison of classical and TFA methods for the peak frequency estimation.

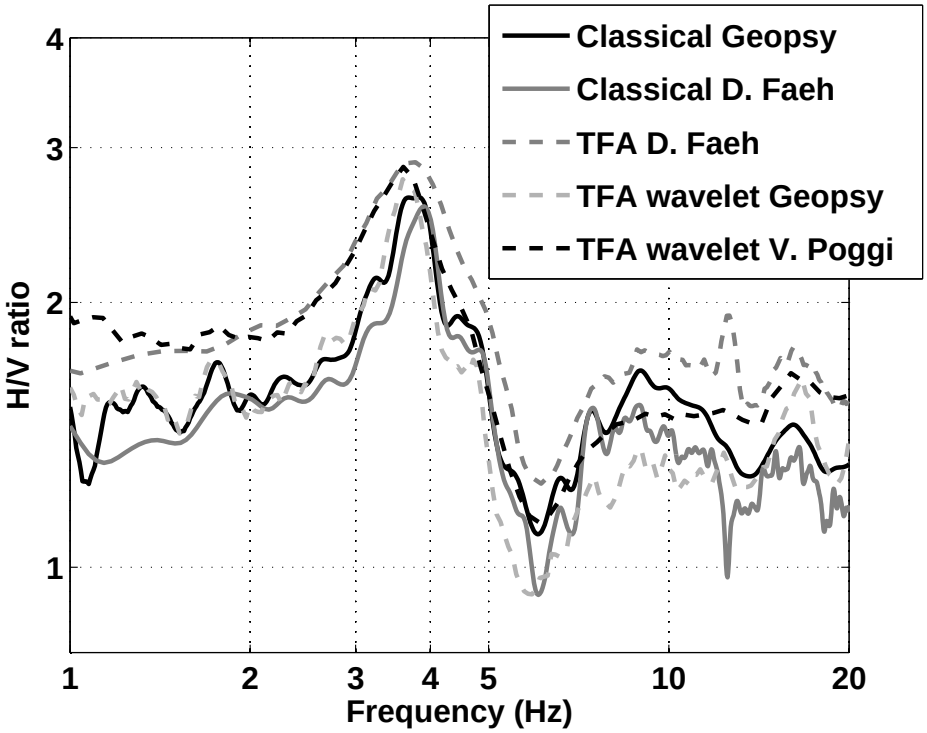

Figure 7: H/V spectral ratios for point BUA000 using the different codes. Classical methods were divided by $\sqrt{2}$.

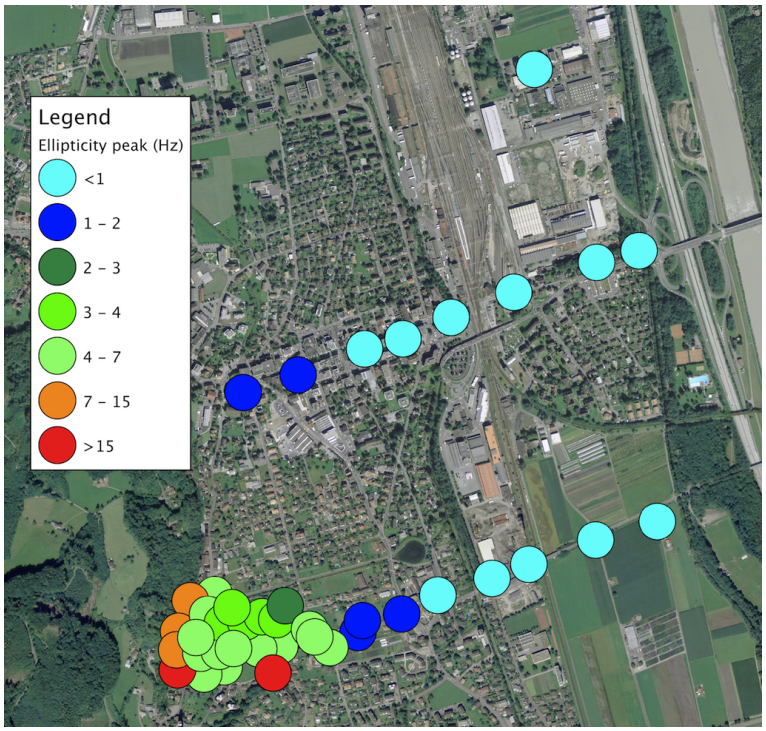

Figure 8: Map of the peak frequency of the ellipticity function.

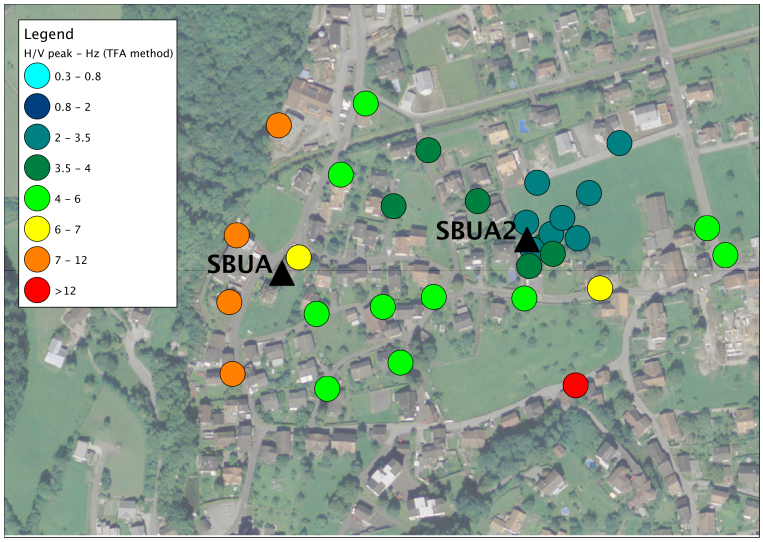

Figure 9: Map of the peak frequency of the H/V ratio in the area of the SBUA2 station.

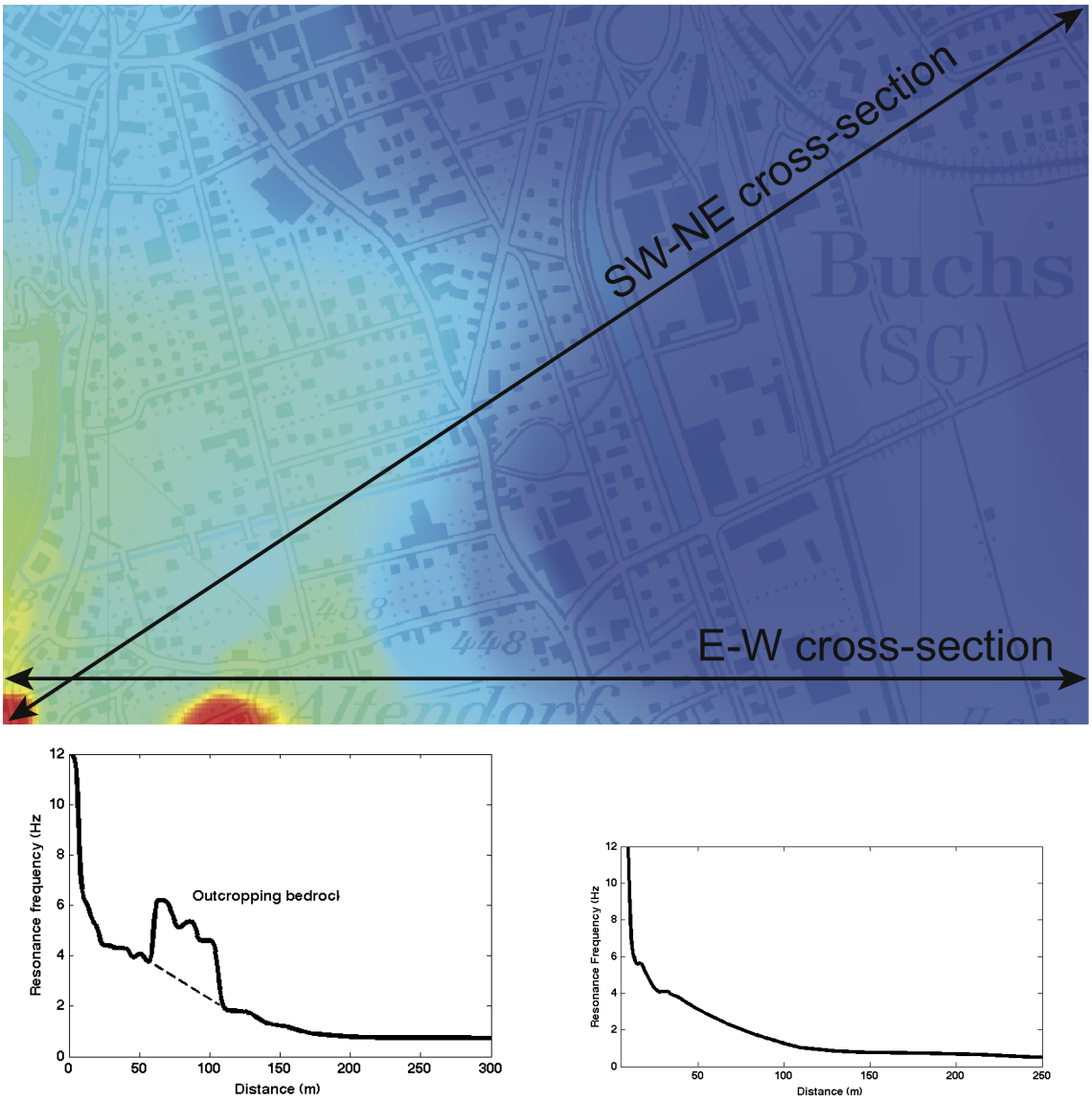

Figure 10: Interpolated resonance frequencies in Buchs and 2 cross-sections (left: E-W and right: SW-NE).

4.3 Boreholes

Boreholes exist close to the investigated site (Fig. 11) for the installation of a heat pump and provided by the Amt für Umwelt und Energie of Kanton St. Gallen. Unfortunately, no data for boreholes 304541 and 314540 were available. Borehole 305375 is very close to the array centre and the SBUA2 station but unfortunately only $65\,\mathrm{m}$ deep. Boreholes 304811 and 314568 are close one another ($70\,\mathrm{m}$) and deeper 120 and $85\,\mathrm{m}$ but located further South to the investigated area, outside of the assumed alluvial fan. However, their interpretation presented Fig. 12, shows that the bedrock, made of limestone, is dipping quite rapidly under the sediments in between the two boreholes ($100\,\mathrm{m}$ from the basin edge), where the Rhine sediments appear. This is probably due to the glacial erosion when the glacier was in the river bed. This slope explains the rapid change of the H/V peak in this region (from 4.6 to $1.8\,\mathrm{Hz}$ see section on H/V measurements).

In the investigated area, the borehole shows $65\,\mathrm{m}$ of gravels (Fig. 13). No clear interface can be extracted from the log. On the contrary to the provided document (Fig. 13) that interprets these gravels as fluvial (Rhine), the other boreholes tend to show all these gravels are part of the alluvial fan. Assuming the same slope of the bedrock as in Fig. 12 (20°), the array centre being located $240\,\mathrm{m}$ from the basin edge, one can extrapolate around $90\,\mathrm{m}$ of sediments in the alluvial fan.

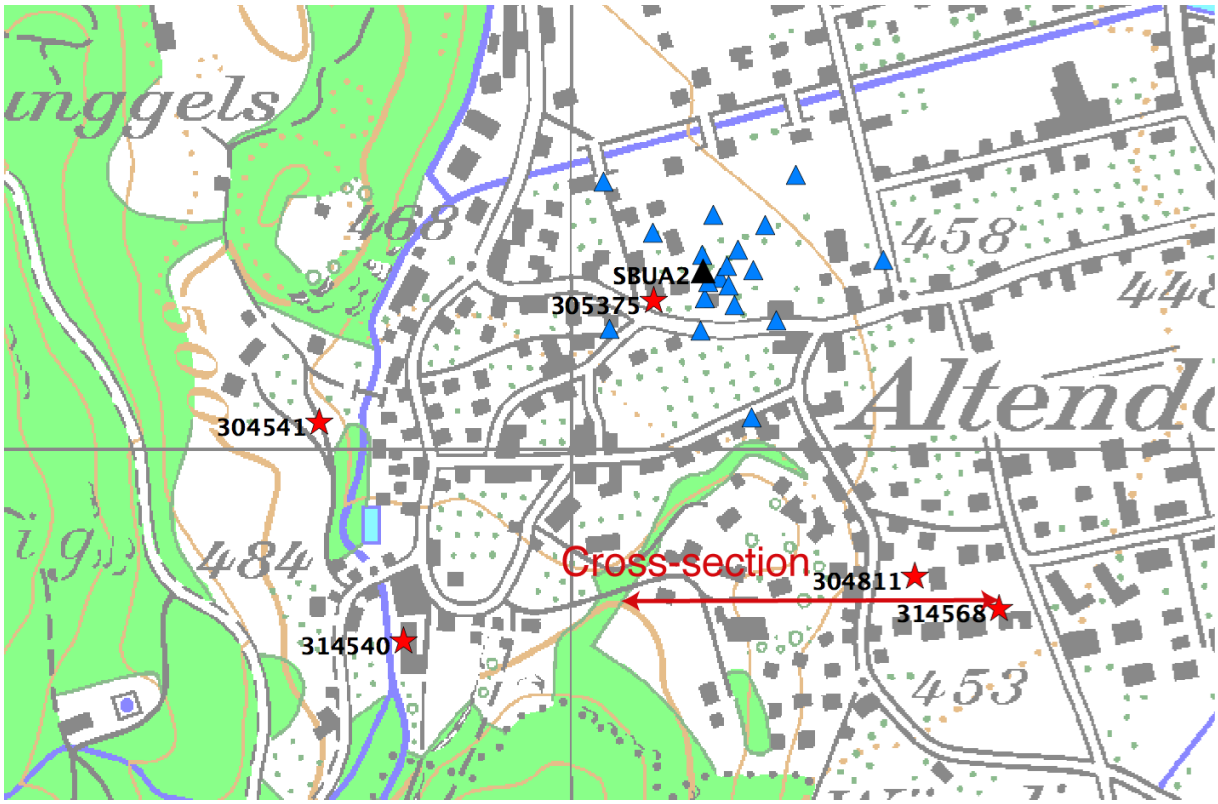

Figure 11: Location of available boreholes (red stars), the array stations (blue triangles) and the cross-section for borehole interpolation (Fig. 12).

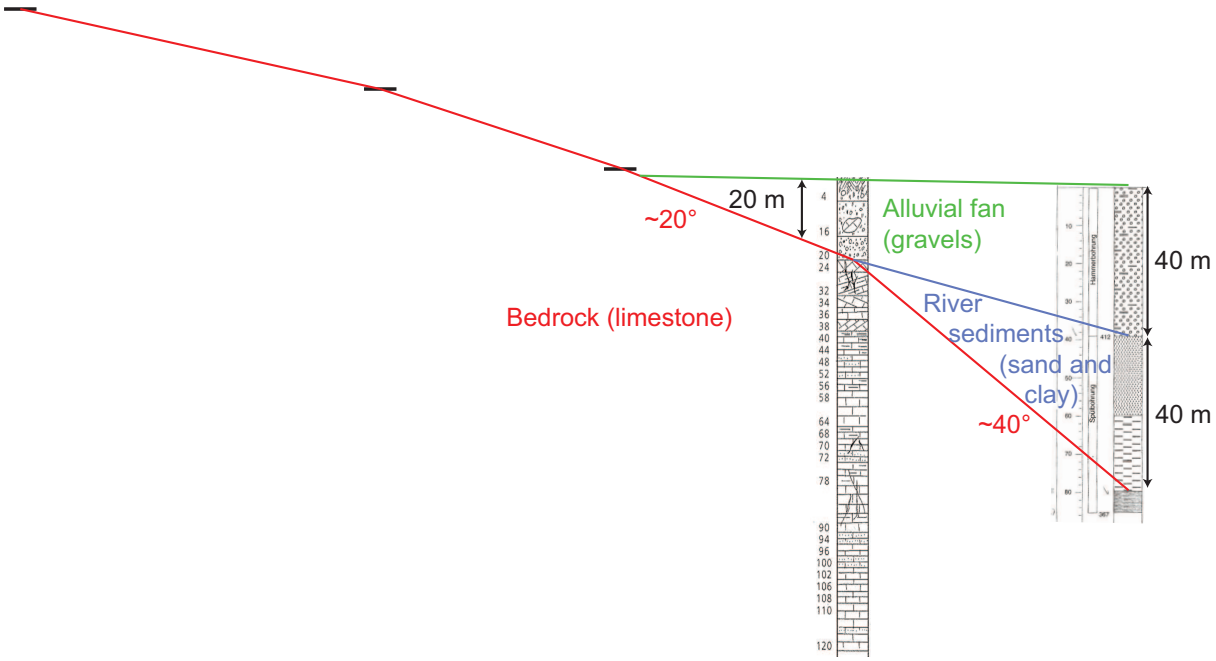

Figure 12: Interpretation in section of the basin edge at boreholes 304811 and 314568

Tiefe m u.T.	Profil 1:500	Beschreibung des Bohrgutes	geologische Identifikation
2		grauer Fein- bis Grobkies	
4		grauer Fein- und Grobkies	
6		grauer Grobkies	
10		dunkelgrauer Feinkies	
20		grauer Mittel- bis Grobkies mit Blöcken	"junger" Rheinschotter
28		grauer Mittel- bis Grobkies	
36		grauer Fein- bis Mittelkies	Hinterwasserablagerungen
38		grauer Fein- und Grobkies	
52		grauer Fein- bis Mittelkies schwarzer Kieselkalk, wenig grüner Feinsandstein mit Glaukonit, und selten roter Quarzsandstein	
64		hellgrauer Fein- bis Mittelkies	Rheinschotter
65		grauer Fein- und Grobkies	

Figure 13: Log of the borehole close to the SBUA2 station.

4.4 Bedrock depth from H/V results

Assuming the H/V peak is related to the sediment/bedrock interface, one can estimate the bedrock depth distribution from the peak frequency. Assuming the classical formula $H = \frac{V_s}{4f_0}$, with $V_s = 500\,\mathrm{m/s}$ (realistic average value across the valley), one can have an idea of the bedrock depth (Fig. 14). More than the absolute value that is biased by the changes in velocity, the shape of the edge is the most interesting with an average slope of 40°, which is relatively steep and coherent with the borehole data (see report on array measurement). The array was performed in the first part of the curve where the slope of the bedrock is not too steep (average slope 20-30°), what is also coherent with the borehole data. However, the velocity of the alluvial fan sediments is probably rather high ($1300\,\mathrm{m/s}$ according to the following sections), which is probably not the case of the sediments from the Rhine. This is a probable bias of interpreting the inverse of resonance frequencies directly as bedrock depth.

Borehole, topography and H/V measurement lead therefore to the same picture: a bedrock of 20-30° dipping under the alluvial fan and then an abrupt change in the slope of the bedrock (40°) dipping under the Rhine sediments. In the middle of the valley the bedrock depth does not vary much. This U-shape is typical of glacial valleys.

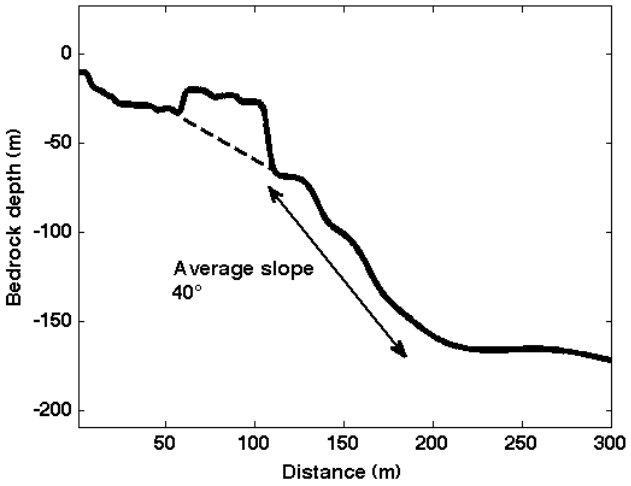

Figure 14: Estimated shape of the bedrock depth from the E-W cross-section using simplistic assumptions.

4.5 Site to reference ratios (Amplification function)

As the H/V processing showed that point BUA403 was probably on rock, the spectral ratios of the horizontal components (square root of the sum) between all recordings of dataset 3 (night recording) and recording at point BUA403 could be computed on ambient vibrations. For that purpose, the average Fourier transform on overlapping tapered windows were computed. The H/V ratios were also recomputed using exactly the same procedure. The results, smoothed using Konno and Ohmachi [1998] (b=80) are presented in Fig. 15. They show a clear amplification of the ground motion of a factor of 5 on average up to 7 between 3 and 12 Hz. This function is not simple and presents several maxima. Comparing the maximum frequency peak of the ratios

with the H/V peak, no good correlation can be found (Fig. 16 left). However, when comparing the first peak in the amplification function (that has not necessarily the highest amplitude) with the H/V peak, the correlation is almost perfect (Fig. 16 right). Fig. 17 shows two examples of comparison between H/V curve and amplification function. H/V is capable of showing the first peak in the amplification function but this peak is not generally the one producing the highest amplification. This amplification function, developed from ambient vibrations, is further compared to the amplification from empirical spectral modeling (ESM) [Edwards et al., 2013] based on small earthquake recordings at station SBUA2 (Fig. 18). In order to use comparable parameters, the ESM function includes the anelastic attenuation and the site-to-reference ratios are corrected to the Swiss reference following Edwards et al. [2013] and assuming a velocity of the local bedrock of $3000\,\mathrm{m/s}$. This comparison is excellent up to $10\,\mathrm{Hz}$.

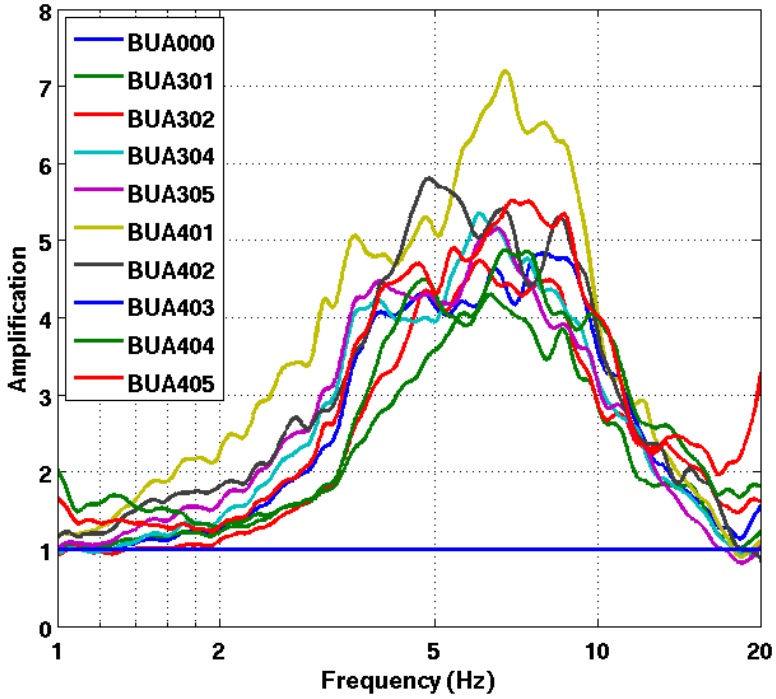

Figure 15: Site over reference spectral ratios.

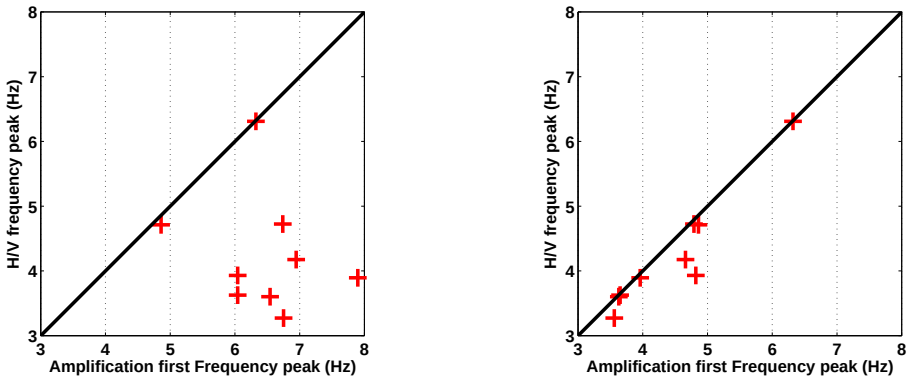

Figure 16: Correlation between the frequency peak in the amplification function and the H/V peak: maximum amplitude peak in the function (left), first peak in the function (right).

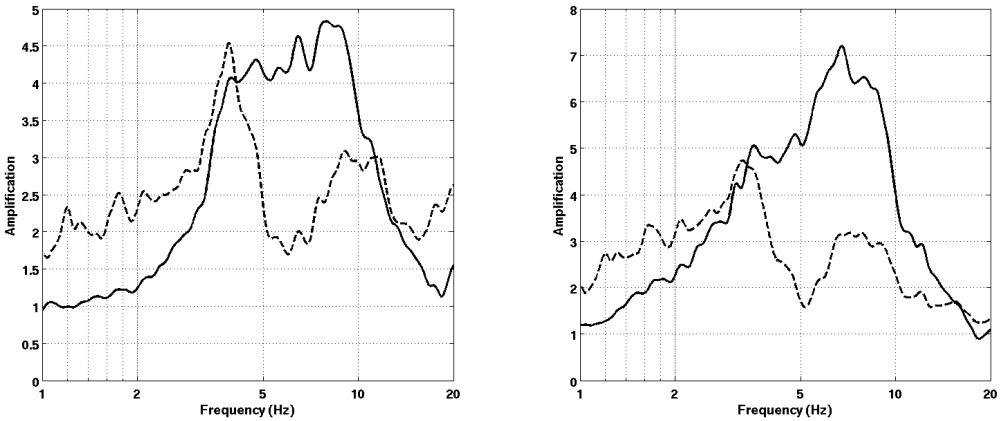

Figure 17: Comparison between the site over reference spectral ratios (solid lines) and the H/V spectral ratios (dashed lines) for points BUA000 (left) and BUA401 (right).

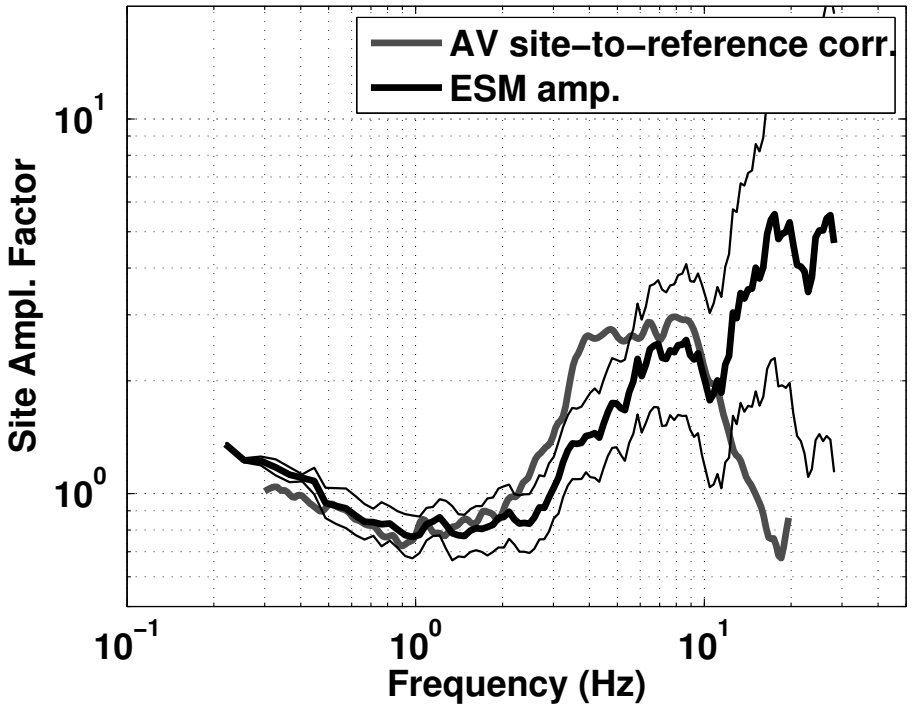

Figure 18: Comparison of the site-to-reference spectral ratios under ambient vibrations at BUA000 and amplification from empirical spectral modeling of earthquake recordings. These amplifications are relative to the Swiss reference.

4.6 Polarization analysis

A polarization analysis using the code of Burjánek et al. [2010] was performed in order to determine if the resonance is polarized and therefore related to 2D/3D resonance. The results show clearly a polarization at the peak frequency between 3 and 4 Hz in the direction 70 °N, corresponding to the axis of the alluvial fan (Fig. 19). This occurs only for all the sensors except sensors BUA402, 403 and 405, i.e. sensors outside the alluvial fan. The H/V peak corresponds therefore to a 2D resonance and the ellipticity information is therefore not used in the 1D inversion.

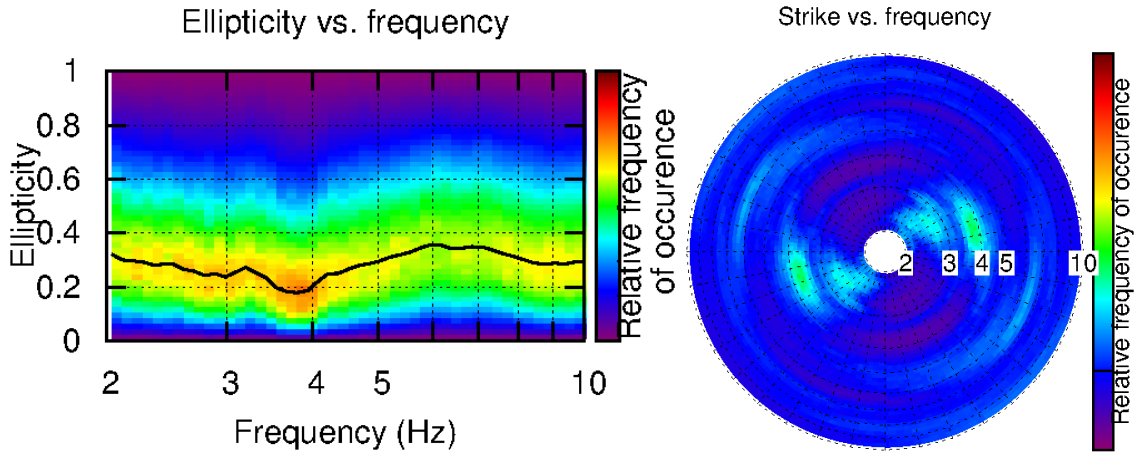

Figure 19: Polarization analysis at point BUA000. Left: Ellipticity (A trough in the ellipticity corresponds to polarized motion). Right: Strike of the polarization.

5 Array processing

5.1 Processing methods and parameters

The vertical components of the arrays were processed using the FK and the High-resolution FK analysis [Capon, 1969] using the Geopsy `http://www.geopsy.org` software. Large time windows were considered (500T) because it gave better results. All the consistent results were concatenated.

Moreover, a 3C array analysis [Fäh et al., 2008] was also performed using the 3C_array_analysis software [Poggi and Fäh, 2010]. It allows to derive Rayleigh and Love modes. The results of computations of both datasets were assembled to estimate the dispersion curves.

Method	Set	Freq. band	Win. length	Anti-trig.	Overlap	Grid step	Grid size	# max.
HRFK 1C	1	$3-25\,\mathrm{Hz}$	$500T$	No	50%	0.002	0.6	3
FK 1C	1	$3-25\,\mathrm{Hz}$	$500T$	No	50%	0.002	0.6	3
HRFK 1C	2	$3-25\,\mathrm{Hz}$	$500T$	No	50%	0.001	0.3	3
HRFK 1C	3	$3-25\,\mathrm{Hz}$	$500T$	No	50%	0.001	0.3	3
HRFK 3C	1	$2-25\,\mathrm{Hz}$	Wav. 10 Tap. 0.2	No	50%	300 m/s	3000 m/s	5
HRFK 3C	2	$2-25\,\mathrm{Hz}$	Wav. 10 Tap. 0.2	No	50%	300 m/s	3000 m/s	5

Table 5: Methods and parameters used for the array processing.

5.2 Obtained dispersion curves

The first mode (Rayleigh) in the 1C FK analysis could be picked between 5.5 and $21\,\mathrm{Hz}$ (Fig. 20) including its standard deviation. The velocities are high from $1700\,\mathrm{m/s}$ at $5.5\,\mathrm{Hz}$ down to $440\,\mathrm{m/s}$ at $21\,\mathrm{Hz}$.

Using the 3C component (Fig. 21), another interpretation of the Rayleigh modes is made: considering also the radial component, the kink at $13\,\mathrm{Hz}$ is believed not to belong to the fundamental mode but to the first higher mode. The fundamental Love mode can also be picked. Rayleigh mode is picked from 5 to $21\,\mathrm{Hz}$ and Love from 4 to $21\,\mathrm{Hz}$. At low frequencies, the picking is not obvious and may differ depending on the used dataset. It may either be due to lateral heterogeneity (the large rings do not sample the same area) or to array limits.

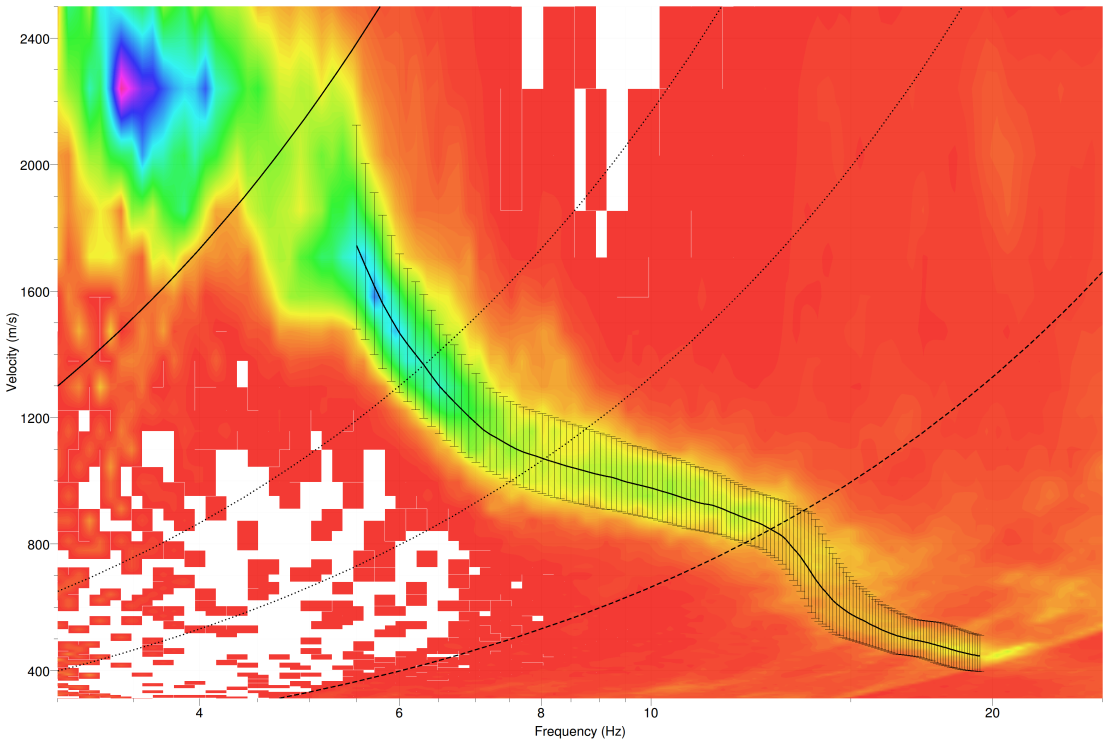

Figure 20: Dispersion curve obtained from the 1C array analysis.

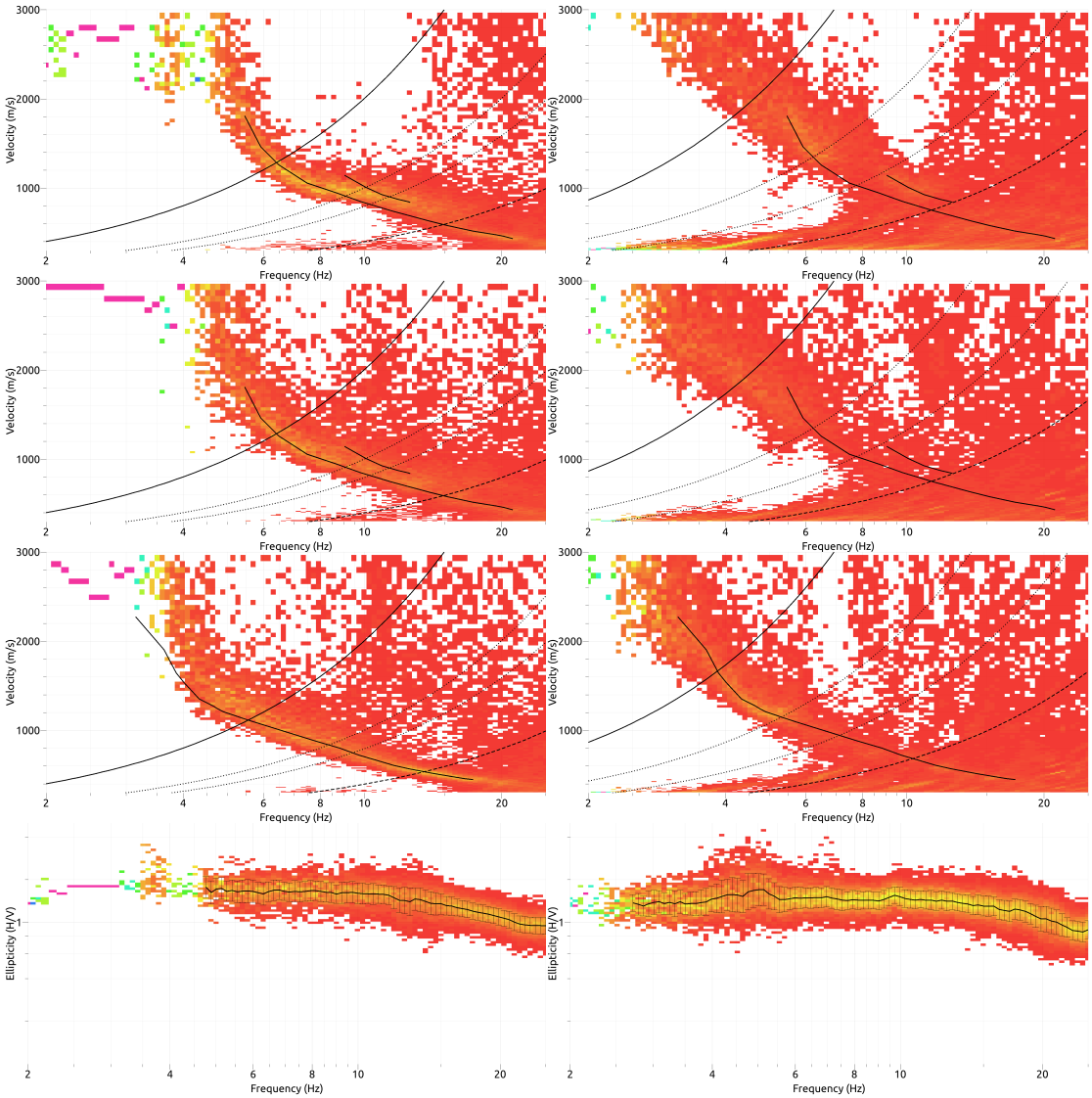

Figure 21: Dispersion curves (from top to bottom: vertical, radial, transverse) and ellipticity obtained from the 3C array analysis (left: first configuration; right: second configuration).

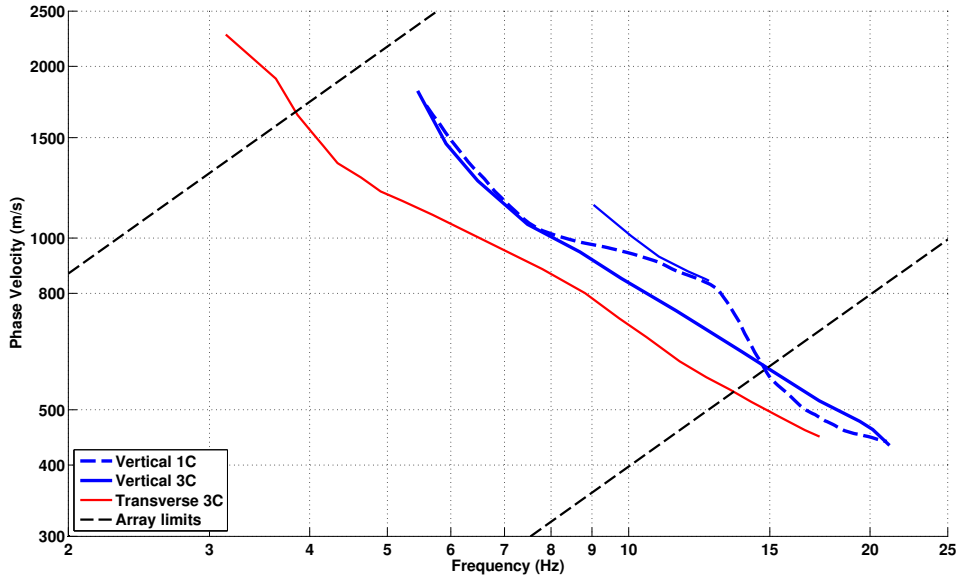

Figure 22: Comparison of obtained dispersion curves using 1C and 3C analyses.

6 Inversion and interpretation

6.1 Inversion

For the inversion, the Love and Rayleigh fundamental modes dispersion curves and the first Rayleigh higher modes (3C analysis) without standard deviation to avoid different weighting were used as simultaneous targets. The ellipticity information is not used due to the strong polarization of its peak frequency probably due to 2D resonance. All curves were resampled using 50 points between 2 and 23 Hz in log scale.

The inversion was performed using the Improved Neighborhood Algorithm (NA) [Wathelet, 2008] implemented in the Dinver software. In this algorithm, the tuning parameters are the following: Ns_0 is the number of starting models, randomly distributed in the parameter space, Nr is the the number of best cells considered around these Ns_0 models, Ns is the number of new cells generated in the neighborhood of the Nr cells (Ns/Nr per cell) and It_{max} is the number of iteration of this process. The process ends with $Ns_0 + Nr * \frac{Ns}{Nr} * It_{max}$ models. The used parameters are detailed in Tab. 6.

It_{max}	Ns_0	Ns	Nr
500	10000	100	100

Table 6: Tuning parameters of Neighborhood Algorithm.

During the inversion process, low velocity zones were not allowed. The Poisson ratio was inverted in each layer in the range 0.2-0.4, up to 0.45 just below the assumed water table. The density was supposed equal to $2000\,\mathrm{kg/m^3}$ except for the last layer ($2400\,\mathrm{kg/m^3}$). Since no ellipticity information could be used to invert the bedrock depth, it was fixed from the topographical constraints at $90\,\mathrm{m}$. Inversions with free layer depths as well as fixed layer depths were performed. 3 layers are enough to explain most of the targets (dispersion and ellipticity), but more layers are used to smooth the obtained results and better explore the parameter space. 5 independent runs of 5 different parametrization schemes (3, 4 and 5 layers over a half space and 8 and 11 layers with fixed depth) were performed. For further elaborations, the best models of these 25 runs were selected (Fig. 25).

The velocity is gradually increasing with depth down to $50\,\mathrm{m}$ from 150 to $1300\,\mathrm{m/s}$ without clear layering. These results are therefore consistent with the borehole data that show no change of material (gravels). At this depth, a layer with constant velocity (around $1300\,\mathrm{m/s}$) is found down to the bedrock. The velocity in the bedrock is poorly constraint at a value of $3000\,\mathrm{m/s}$.

When comparing to the target curves (Fig. 23), the Love and Rayleigh fundamental dispersion curves are well represented. The first higher Rayleigh mode is misplaced. It may be due to the fact that, in the FK analysis, the energy of both modes is mixed in between the actual curves. It is clear that the 1D assumption when deriving the dispersion curves was not perfectly fulfilled so that these curves are not certain. The ellipticity is very different from the H/V curve, probably more representative of the amplification function.

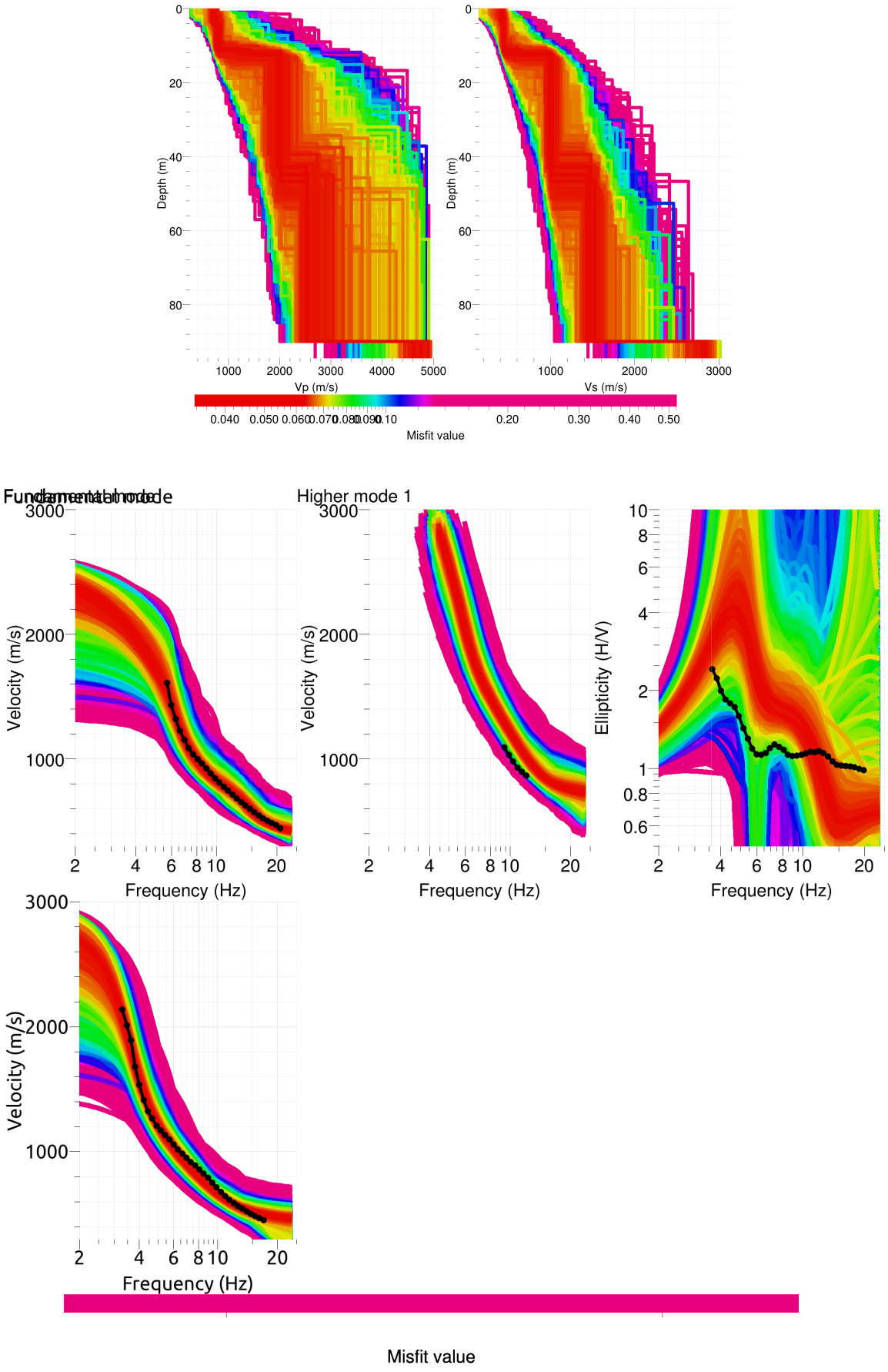

Figure 23: Inverted ground profiles in terms of V_p and V_s (top) and comparison between inverted models and measured Rayleigh and Love modes and corresponding ellipticity, free layer depth strategy.

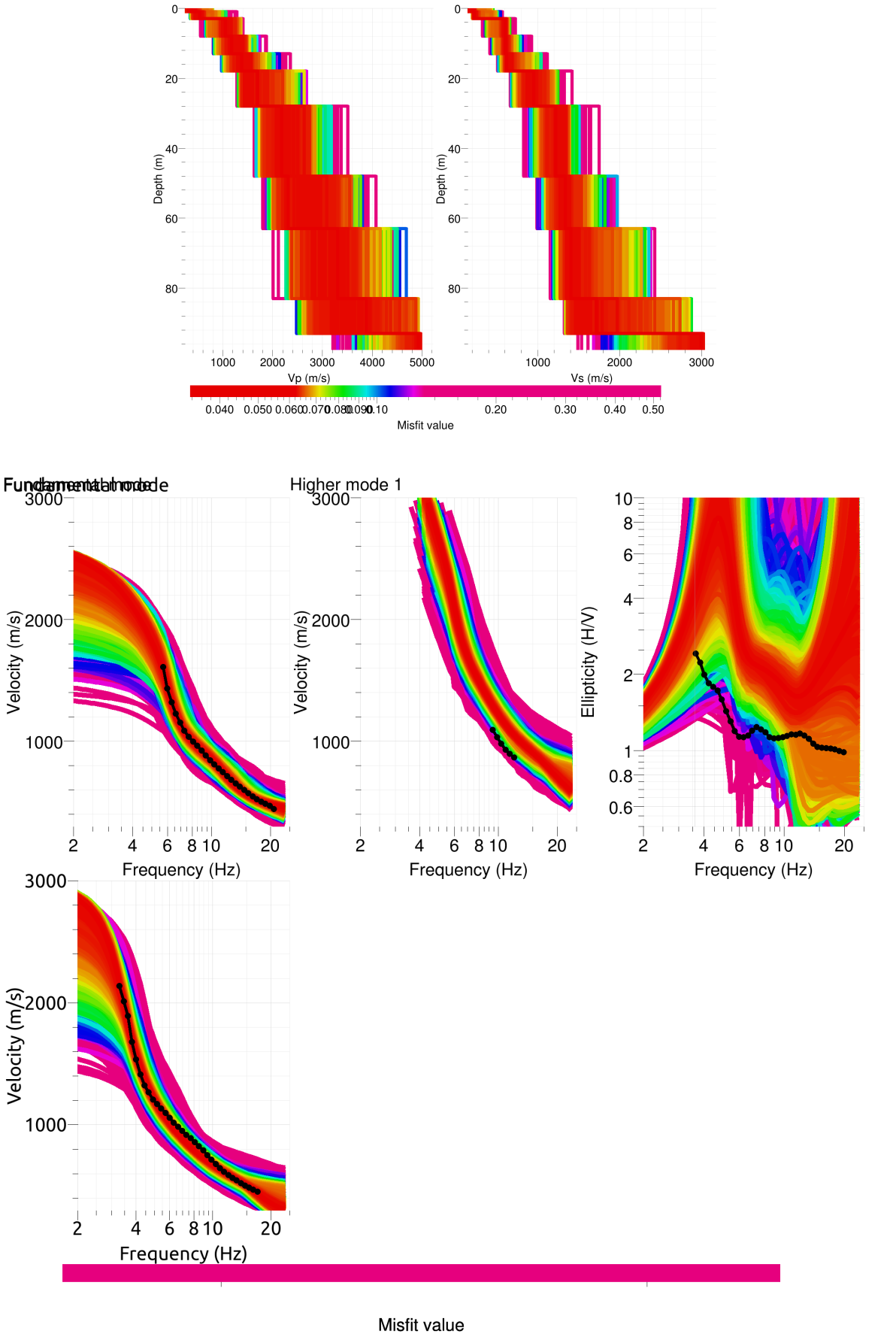

Figure 24: Inverted ground profiles in terms of V_p and V_s (top) and comparison between inverted models and measured Rayleigh and Love modes and corresponding ellipticity, fixed layer depth strategy.

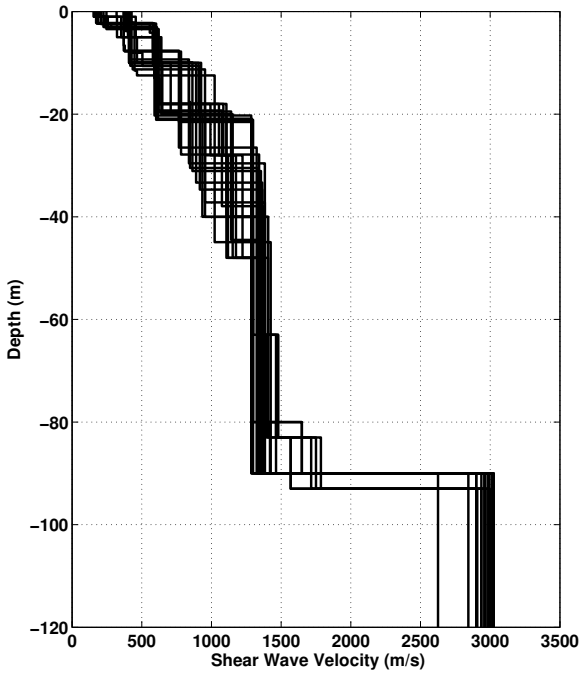

Figure 25: V_s ground profiles for the selected 25 best models.

6.2 Travel time average velocities and ground type

The distribution of the travel time average velocities at different depths was computed from the selected models. The uncertainty, computed as the standard deviation of the distribution of travel time average velocities for the considered models, is also provided, but its meaning is doubtful. $V_{s,30}$ is found to be $618\,\mathrm{m/s}$, meaning the site can be classified as class B in the Eurocode 8 [CEN, 2004]. Considering the Swiss Code SIA261 [SIA, 2003], the website `http://erdbeben.admin.ch` considers this site, as well as the whole Rhine valley as class C. However, considering these results, this site should be considered as class B.

	Mean (m/s)	**Uncertainty (m/s)**
$V_{s,5}$	344	58
$V_{s,10}$	405	17
$V_{s,20}$	519	37
$V_{s,30}$	618	24
$V_{s,40}$	700	20
$V_{s,50}$	771	22
$V_{s,100}$	1025	22
$V_{s,150}$	-	-
$V_{s,200}$	-	-

Table 7: Travel time averages at different depths from the inverted models. Uncertainty is given as one standard deviation from the selected profiles.

6.3 SH transfer function and quarter-wavelength velocity

The quarter-wavelength velocity approach [Joyner et al., 1981] provides, for a given frequency, the average velocity at a depth corresponding to 1/4 of the wavelength of interest. It is useful to identify the frequency limits of the experimental data (minimum frequency in dispersion curves at $3.2\,\mathrm{Hz}$ here). The results using this proxy show that the dispersions curves constrain the profiles down to $70\,\mathrm{m}$ (Fig. 26). Moreover, the quarter wavelength impedance-contrast introduced by Poggi et al. [2012] is also displayed in the figure. It corresponds to the ratio between two quarter-wavelength average velocities, respectively from the top and the bottom part of the velocity profile, at a given frequency [Poggi et al., 2012]. It shows a trough (inverse shows a peak) at the resonance frequency (too low for this figure).
Moreover, the theoretical SH-wave transfer function for vertical propagation [Roesset, 1970] is computed from the inverted profiles. It is compared to the quarter-wavelength amplification [Joyner et al., 1981], that however cannot take resonances into account (Fig. 27). In this case, the models are predicting an amplification up to a factor of 6 at the resonance frequency $3.6\,\mathrm{Hz}$ and especially at $8.3\,\mathrm{Hz}$. They are compared to the amplification function retrieved from ambient vibrations (site-to-reference) on Fig. 28. This curve includes the mean plus/minus a standard deviation over the array points.

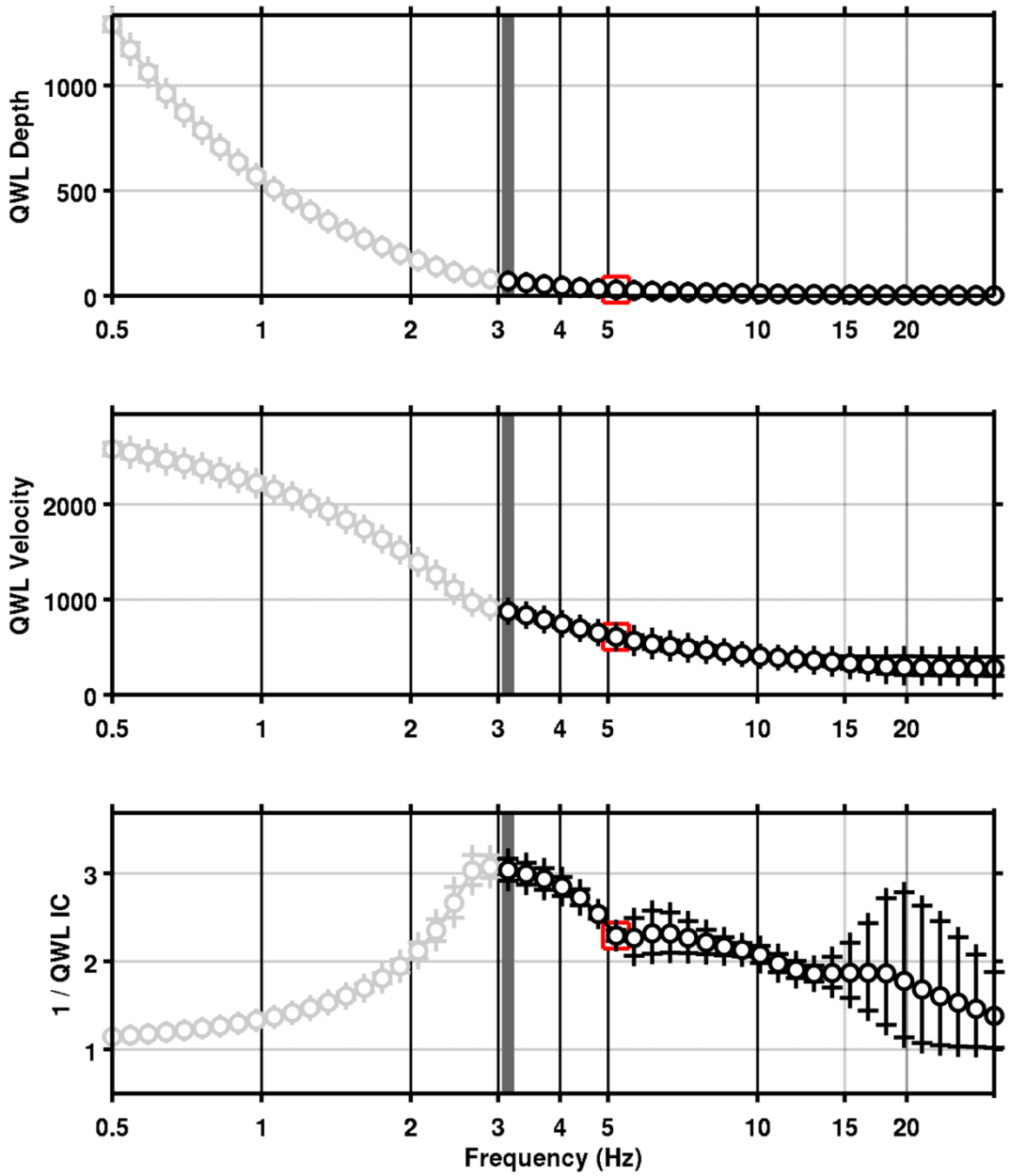

Figure 26: Quarter wavelength velocity representation of the velocity profile (top: depth, centre: velocity, bottom: inverse of the impedance contrast). Black curve is constrained by the dispersion curves, light grey is not constrained by the data. Red square is corresponding to $V_{s,30}$.

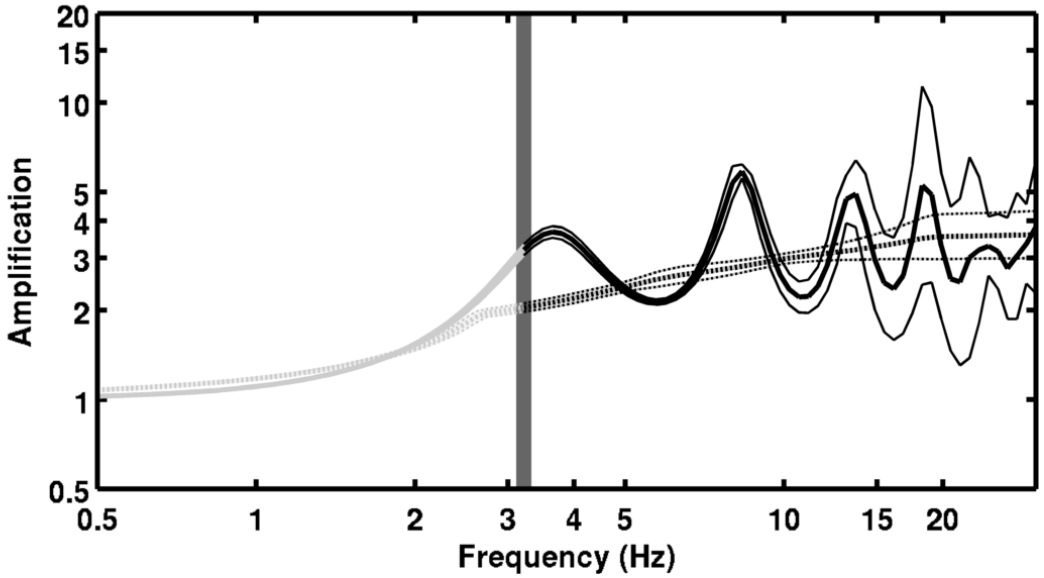

Figure 27: Theoretical SH transfer function (solid line) and quarter wavelength impedance contrast (dashed line) with their standard deviation. Significance of the greyshades is detailed in Fig. 26.

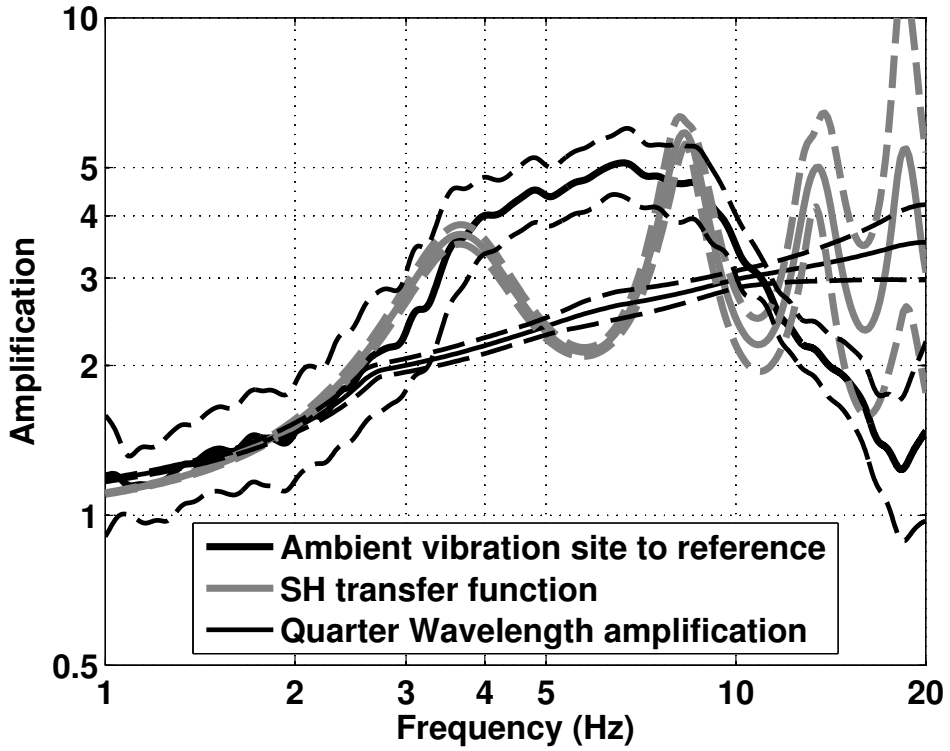

Figure 28: Theoretical SH transfer function versus quarter wavelength proxy for the amplification and observed amplification function under ambient vibrations (local reference).

7 Conclusions

These array measurements were successful in deriving a velocity model for the alluvial fan of Buchs Altendorf. At the central point of the array, we found a gradually increasing velocity with depth down to $50\,\mathrm{m}$ from 150 to $1300\,\mathrm{m/s}$ without clear layering corresponding to more and more consolidated gravels. At this depth, a layer with constant velocity (around $1300\,\mathrm{m/s}$) is found down to the bedrock at $90\,\mathrm{m}$. The velocity in the bedrock is poorly constraint at a value of $3000\,\mathrm{m/s}$. The derived layers are very stiff and explain the H/V peak at $3.6\,\mathrm{Hz}$ that corresponds to the fundamental SH resonance frequency, but not the ellipticity. $V_{s,30}$ is found to be close to $620\,\mathrm{m/s}$. A site to reference analysis from the array data using ambient vibrations and compared to earthquake recordings at the station could also show several amplification peaks, the first being related to the interface with the bedrock. The following peaks produce the largest amplifications up to 7 (5 in the centre of the array) at higher frequencies (6 to $8\,\mathrm{Hz}$). Comparing with the SH transfer function and using polarization analysis, it seems that part of the recorded motion is due to a local 2D resonance.

The H/V study allowed to map the fundamental frequency around Buchs-Altendorf and in the central part of the Rhine valley. They represent the bedrock depth but since the velocities are much different along the profile, the absolute values are difficult to interpret. In the alluvial fan, the rapid changes in the resonance frequency may also be due to the resonance of different interfaces. On overall, the bedrock is found to show a U-shape under the Rhine sediments, with a much steeper slope than the outcropping rock topography and the bedrock slope under the alluvial fan. This shape is typical of the glacial valleys.

Thanks to the different processing of the ambient vibration array (H/V, site to reference and array analysis), the borehole data and the additional H/V points, the site SBUA is well characterized in terms of 1D velocity profile and 3D mapping of the bedrock.

Acknowledgements

The authors thank Marco Terzic for the single station measurements, Stefano Marano for the help during these measurements and the Amt für Umwelt und Energie of Kanton St. Gallen for providing the boreholes. The authors also thank Daniel Gilgen and Franz Weber for design of the realtime system.

References

Sylvette Bonnefoy-Claudet, Fabrice Cotton, and Pierre-Yves Bard. The nature of noise wavefield and its applications for site effects studies. *Earth-Science Reviews*, 79(3-4): 205–227, December 2006. ISSN 00128252. doi: 10.1016/j.earscirev.2006.07.004. URL http://linkinghub.elsevier.com/retrieve/pii/S0012825206001012.

Jan Burjánek, Gabriela Gassner-Stamm, Valerio Poggi, Jeffrey R. Moore, and Donat Fäh. Ambient vibration analysis of an unstable mountain slope. *Geophysical Journal International*, 180(2):820–828, February 2010. ISSN 0956540X. doi: 10.1111/j.1365-246X.2009.04451.x. URL http://doi.wiley.com/10.1111/j.1365-246X.2009.04451.x.

J. Capon. High-Resolution Frequency-Wavenumber Spectrum Analysis. *Proceedings of the IEEE*, 57(8):1408–1418, 1969.

CEN. *Eurocode 8: Design of structures for earthquake resistance - Part 1: General rules, seismic actions and rules for buildings*. European Committee for Standardization, en 1998-1: edition, 2004.

Benjamin Edwards, Clotaire Michel, Valerio Poggi, and D. Fah. Determination of Site Amplification from Regional Seismicity: Application to the Swiss National Seismic Networks. *Seismological Research Letters*, 84(4):611–621, July 2013. ISSN 0895-0695. doi: 10.1785/0220120176. URL http://srl.geoscienceworld.org/cgi/doi/10.1785/0220120176.

Donat Fäh, Fortunat Kind, and Domenico Giardini. A theoretical investigation of average H / V ratios. *Geophysical Journal International*, 145:535–549, 2001.

Donat Fäh, Gabriela Stamm, and Hans-Balder Havenith. Analysis of three-component ambient vibration array measurements. *Geophysical Journal International*, 172(1):199–213, January 2008. ISSN 0956540X. doi: 10.1111/j.1365-246X.2007.03625.x. URL http://doi.wiley.com/10.1111/j.1365-246X.2007.03625.x.

Donat Fäh, Marc Wathelet, Miriam Kristekova, Hans-Balder Havenith, Brigitte Endrun, Gabriela Stamm, Valerio Poggi, Jan Burjanek, and Cécile Cornou. Using Ellipticity Information for Site Characterisation Using Ellipticity Information for Site Characterisation. Technical report, NERIES JRA4 Task B2, 2009.

William B. Joyner, Richard E. Warrick, and Thomas E. Fumal. The effect of Quaternary alluvium on strong ground motion in the Coyote Lake, California, earthquake of 1979. *Bulletin of the Seismological Society of America*, 71(4):1333–1349, 1981.

Katsuaki Konno and Tatsuo Ohmachi. Ground-Motion Characteristics Estimated from Spectral Ratio between Horizontal and Vertical Components of Microtremor. *Bulletin of the Seismological Society of America*, 88(1):228–241, 1998.

Valerio Poggi and Donat Fäh. Estimating Rayleigh wave particle motion from three-component array analysis of ambient vibrations. *Geophysical Journal International*, 180(1):251–267, January 2010. ISSN 0956540X. doi: 10.1111/j.1365-246X.2009.04402.x. URL http://doi.wiley.com/10.1111/j.1365-246X.2009.04402.x.

Valerio Poggi, Benjamin Edwards, and D. Fah. Characterizing the Vertical-to-Horizontal Ratio of Ground Motion at Soft-Sediment Sites. *Bulletin of the Seismological Society of America*, 102(6):2741–2756, December 2012. ISSN 0037-1106. doi: 10.1785/0120120039. URL http://www.bssaonline.org/cgi/doi/10.1785/0120120039.

J.M. Roesset. Fundamentals of soil amplification. In R. J. Hansen, editor, *Seismic Design for Nuclear Power Plants*, pages 183–244. M.I.T. Press, Cambridge, Mass., 1970. ISBN 978-0-262-08041-5. URL http://mitpress.mit.edu/catalog/item/default.asp?ttype=2\&tid=5998.

SIA. *SIA 261 Actions sur les structures porteuses*. Société suisse des ingénieurs et des architectes, Zürich, sia 261:20 edition, 2003.

Marc Wathelet. An improved neighborhood algorithm: Parameter conditions and dynamic scaling. *Geophysical Research Letters*, 35(9):1–5, May 2008. ISSN 0094-8276. doi: 10.1029/2008GL033256. URL http://www.agu.org/pubs/crossref/2008/2008GL033256.shtml.